Large Negative Poisson's Ratio and Anisotropic Mechanics in New Penta-PBN Monolayer

Shambhu Bhandari Sharma,* Issam A. Qattan,* Santosh KC, and Ahmad M. Alsaad

Read Online

ACCESS | Metrics & More | Article Recommendations | Supporting Information

ABSTRACT: The scarce negative Poisson's ratio (NPR) in a two-dimensional (2D) material is an exceptional auxetic property that offers an opportunity to develop nanoscale futuristic multi-functional devices and has been drawing extensive research interest. Inspired by the buckled pentagonal iso-structures that often expose NPR, we employ state-of-the-art first-principles density functional theory calculations and analyses to predict a new 2D metallic ternary auxetic penta-phosphorus boron nitride (p-PBN) with a high value of NPR. The new p-PBN is stable structurally, mechanically, and dynamically and sustainable at room temperature, with experimental feasibility. The short and strong quasi sp³-hybridized B−N bond and unique bond variation and geometrical reconstruction with an applied strain allow p-PBN to inherit a high value of NPR (−0.236) along the (010) direction, the highest among any other ternary penta iso-structures reported to date. Despite having a small elastic strength, the highly asymmetric Young's modulus and Poisson's ratio along the (100) and (010) directions indicate large anisotropic mechanics, which are crucial for potential applications in nanomechanics and nanoauxetics.
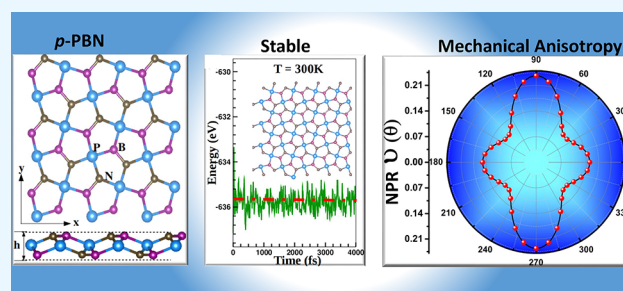
INTRODUCTION

In recent years, a new class of two-dimensional (2D) Cairo-pentagonal lattice monolayers and their one-dimensional (1D) nanoribbon are drawing considerable attention due to their extraordinary chemical and physical properties[1,2] identified by both experiments[3−6] and theories.[7−13] Unlike ultra-thin planar hexagonal graphene,[14] the low-symmetric, trilayered, and buckled geometry of penta monolayers allow them more degrees of freedom to possess novel mechanical, piezoelectric, electronic, thermal, and optical properties.[3−13] In addition, the inheritance of the robust band topology and visible light-harvesting direct-band gap semiconducting to metallic electronic behavior of penta monolayers make them highly desirable in cutting-edge technological devices such as optomechanical sensors, lithium-ion batteries, and solar cells.[11,15,16]

Particularly, the finding of a very rare mechanical behavior, the negative Poisson's ratio (NPR), from the first penta monolayer, monoelemental penta-graphene,[17] to a binary,[18−20] up to a ternary[7,9] penta monolayer shows tremendous possibilities of NPR, which is attributed to the unique buckled/puckered geometry and deformation mechanism dominated by the inter-atomic interactions.

Unlike the positive Poisson's ratio material, NPR materials shrink (expand) laterally when compressed (stretched) axially and transform into a dome −shape, while the out-of-plane bending moment is applied.[21] Most of these materials manifest NPR values ranging from −1 to 0. However, some materials such as AlP exhibited a large NPR value of −1.779.[22] The higher the NPR value, the more lateral to longitudinal expansion and contraction the material undergoes. High NPR materials have a higher indentation, impact, and crack-propagation resistance with superior sound absorption performance.[23,24] These excellent properties allow NPR materials to have broad applications in the automotive, aerospace, marine, and other industrial fields.[25] More specifically, they hold great promise in advanced applications such as sensors, biomedicine, fasteners, bullet-proof shields, sports equipment, tissue engineering, and an untold number of unrevealed applications.[26−31]

Even though the Gibson theory predicted the auxetic behavior of 2D materials earlier,[32] the experimental and theoretical findings of intrinsic NPR in black phosphorus (−0.027)[33,34] in 2014 inspired the exploration of the different classes of low-dimensional materials. Since then, NPR is reported in several 2D materials[18] including borophane (−0.053),[35] BP_5 (−0.037),[36] TiN,[37] Be_2C (−0.566),[38] 2D Be_5C_2 (−0.041),[39] penta-B_2N_4 (−0.02) and penta-B N_2 (−0.19),[20] penta-graphene (−0.07),[17] and penta-$PdSe_2$ (−0.022),[19] most of which have puckered and/or buckled
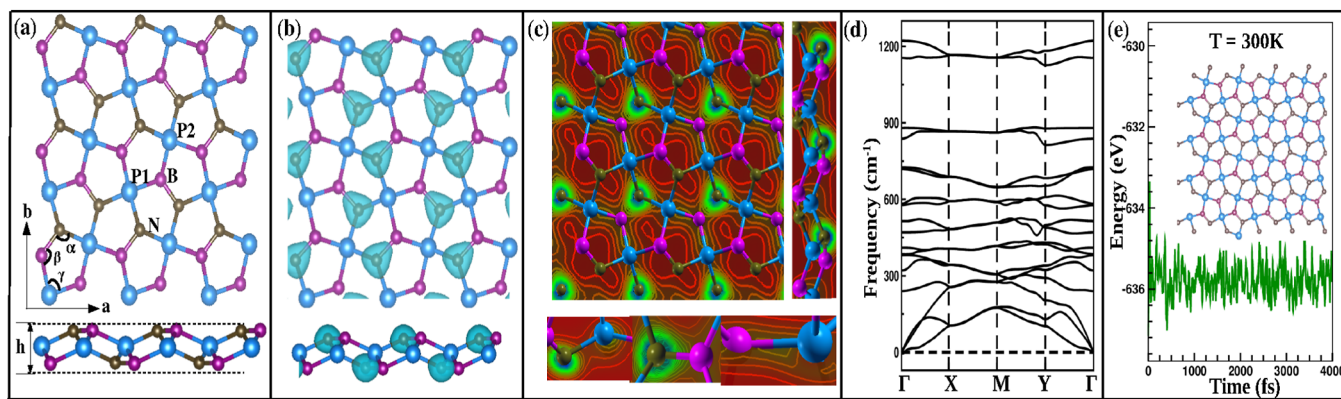
Figure 1. (Color online) (a) fully optimized *p*-PBN monolayer ($4 \times 4 \times 1$ supercell). The blue, magenta, and gray balls represent the P, B, and N atoms, respectively, (b) charge density iso-surface ($0.05 \; e/\text{Å}^3$), (c) charge density contour plots with different viewpoints including a magnified view of charge distribution between atoms (bottom), (d) phonon dispersion of the optimized *p*-PBN, and (e) AIMD simulation at $T = 300$ K for the energy fluctuation as a function of time. The inset shows the top view of the final *p*-PBN structure.

configurations. One of many, pentagonal monolayers are reported to be highly favorable structures for NPR due to their unique geometry and inter-atomic interaction.[18]

Besides Raman spectroscopy,[18] the current experimental efforts to synthesize 2D auxetic materials are still premature, challenging, and lagging behind the theoretical studies.[7] Nevertheless, the synthesis of such 2D auxetic materials is fascinating, highly desirable, and expected to prosper with the advancement of technologies in the near future.

Understanding the exceptional properties of NPR materials as well as their diverse applicabilities in non-planar structures, pentagonal monolayer research is not only limited to device characterization but also creates opportunities for new material designs with sophisticated functionalities. Moving beyond monoelemental penta-graphene to the binary up to the new ternary, still, an untold number of new materials are waiting to be revealed. The quest for a new stable and experimentally feasible auxetic material is always very exciting. Particularly, the ternary penta-sheet is of current interest due to its intriguing physical and chemical properties and potential pertinency.[40]

Considering the outstanding legacy and geometrical favors of phosphorus in the puckered lattice configuration and strong chemistry between boron and nitrogen, we combine these ingredients to introduce a new ternary pentagonal monolayer: the penta-phosphorus boron nitride (*p*-PBN). By employing state-of-art first-principles calculations and theoretical investigations, we confirm that *p*-PBN is a structurally, chemically, thermodynamically, mechanically, and dynamically stable and experimentally feasible 2D material. The presence of NPR, 2D Young's modulus, shear modulus, and the ultimate strength/strain along with their stability criterion and shreds of evidence are examined by the variation of bond length and strain energy as a function of applied strain. Additionally, the presence of strong mechanical anisotropy and elastic strength are very exciting for optomechanical, nanomechanics, auxetic, and other advanced applications for both the industrial and scientific communities.

■ RESULTS AND DISCUSSION

Structural Properties. The geometry of *p*-PBN comprises three layers lattice planes, top/bottom with 3-coordinated boron/nitrogen (B_{3c}/N_{3c}) and middle layer with 4-coordinated phosphorus (P_{4c}) following the mother penta-graphene isostructure (Figure 1a). The primitive unit cell consists of 2P, 2B, and 2N atoms (in 1:1:1 proportion) in trilayered, three virtual layers in a monolayer, which are formed by the P, B, and N atoms, buckled form. Here, the designed structure is fully relaxed to achieve the minimum energy, atomic forces, and stresses. The fully relaxed structure maintains the pentagonal symmetry belonging to *P-2₁* symmetry (space group no. 4). The monolayer has a centered rectangular 2D lattice with lattice parameters $a = 4.31$ Å and $b = 4.28$ Å. The lattice parameters of *p*-PBN are equivalent to the recently predicted ternary pentagonal *p*-SiCN.[7] Interestingly, the supercell consists of four distinct irregular pentagonal Cairo tiles replication, which preserves the periodic boundary conditions.

In the primitive cell, the two P atoms have slightly different bond distances from the N atom. Therefore, they are labeled as P1 and P2 for better visualization. The importance of this choice is realized later when explaining the mechanical properties. The stable configuration of *p*-PBN has N−P1, P1−B, B−N, and B−P2 bond lengths of 1.79, 1.89, 1.44, and 1.89 Å, respectively.

Remarkably, the quasi sp³-hybridized B−N bond is even shorter in *p*-PBN than that of the hexagonal sp²-hybridized bond in *h*-BN (1.45 Å).[41] This uniquely shorter bond length plays an important role in the strength, stability, and advanced mechanical responses of the monolayer. Similarly, the thickness (buckling height) of the monolayer (h), calculated by measuring the difference between the vertical extremities of atoms, is 1.41 Å, which is higher than that of penta-graphene (1.20 Å),[17] penta-SiCN (1.24 Å),[7] penta-BCN (1.34 Å),[10] nevertheless smaller than that of penta-CNP (2.41 Å),[9] penta-BP₅ (2.50 Å),[42] and penta-CN₂ (1.52 Å).[8] The measured bond angles of P−N−B (α), N−B−P (β), and B−P−B (γ) are 111.8, 118.6, and 98.2°, respectively.

The Mulliken charge density analysis is performed to corroborate the bonding mechanism and inter-atomic charge distribution in *p*-PBN. The iso-surface plot (Figure 1b) demonstrates that most of the charge is accumulated around the N atom and shared significantly between the B and N atoms compared to that of the N and P atoms. Furthermore, the nature of the chemical bond is analyzed by visualizing the 2D valence charge density contour plot (Figure 1c). Here, the highest charge density is represented by blue > green > orange > red, in that descending order. The presence of a high electronic charge (green) between B and N and the overlapping of concentric lines with the considerable

conjoining of their electronic wavefunctions confirm the covalent bonding similar to that of h-BN.[43,44] In contrast, the smaller overlap of wavefunctions (dumbbell-shaped contour lines) with small charge sharing between P and N indicates partly ionic and covalent P−N bonding. The deformed conjoining contour lines with some charge sharing (faded-green) demonstrate a polar covalent bond in P−B. Chemically, the strength of bonding in p-PBN follows the order B−N > P−N > P−B, which is also tested against the applied strains while explaining the mechanical results. The cohesive energy (E_c) is calculated to examine the average interatomic binding and structural stability of p-PBN using $E_c = (E_{p\text{-PBN}} - 2E_P - 2 E_B - 2 E_N)/6$, where $E_{p\text{-PBN}}$, E_P, E_B, and E_N represent the energy of p-PBN, isolated P, B, and N atoms, respectively. The high negative E_c of −7.42 eV/atom, comparable to that of h-BN (−8.83 eV/atom),[43,45] justifies it as one of the most stable configurations. Furthermore, the formation energy (E_f) is calculated using $E_f = (E_{p\text{-PBN}} - 2E_P^{\text{Bulk}} - 2E_B^{\text{Bulk}} - 2E_N^{\text{Bulk}})/6$, where E_P^{Bulk}, E_B^{Bulk}, and E_N^{Bulk} represent the energy of P, B, and N atoms at their bulk phase, respectively. The computed E_f (1.16 eV/atom) indicates the feasibility of endothermic experimental synthesis of p-PBN. We have also performed formation energy calculations using the energy of atoms from the most stable possible binary (h-BN) and elementary (phosphorene) phases. The calculated E_f of p-PBN using this approach is 1.10 eV/atom, which is equivalent to the results obtained using the bulk-phase approach. However, no binary or other ternary phases were included in the assessment of the thermodynamic stability. In addition, the lattice vibration and corresponding dynamical stability are verified with the presence of real phonon dispersion for the optimized p-PBN (Figure 1d). For the 6 atomic unit cell, 3 acoustic and 15 optical branches with high vibrational frequencies are observed, which are comparable to that of penta-graphene[17] and graphene,[46,47] indicating the relative dynamical stability. To verify the thermal response of p-PBN, the ab initio molecular dynamics (AIMD) simulation is performed at room temperature ($T = 300$ K), with a time step of 1 fs up to 4000 fs (Figure 1e). At this temperature, the structure remains intact without suffering any significant distortion, bond breaking, or melting, indicating robust thermal stability.

Mechanical Properties and Anisotropy. In low-dimensional materials, mechanical stability, strength, and anisotropy are the crucial factors for machinability, material synthesis, and diverse functionality. Keeping that in mind, we investigate the 2D Young's/shear modulus and Poisson's ratio along the x-direction (100) and y-direction (010) directions at different orientations of the lattice. In addition, to identify the anisotropy, important elastic anisotropic indices are evaluated. For this, the relevant second-order elastic constants (C_{ij}) are computed using the strain-energy method.[10] In the standard Voigt notation,[17,48] the strain energy per unit area as a function of strain $U_s(\varepsilon) = E_s(\varepsilon)/\text{area}$ for a 2D sheet is defined as

$$U_s(\varepsilon) = \frac{1}{2}C_{11}\varepsilon_{xx}^2 + \frac{1}{2}C_{22}\varepsilon_{yy}^2 + C_{12}\varepsilon_{xx}\varepsilon_{yy} + 2C_{66}\varepsilon_{xy}^2 \quad (1)$$

where C_{11}, C_{22}, C_{12}, and C_{66} are second-order elastic tensors, and their values are extracted by fitting the energy curves associated with the uniaxial ($\varepsilon_{x/y}$) and biaxial (ε_{xy}) strains.

The Li's elastic anisotropy measurement methods[49] are used to analyze the mechanical anisotropy. The needed anisotropy indices such as the universal A^{SU}, Ranganathan $A^{\text{Ranganathan}}$,[50] and Kube A^{Kube}[51] are expressed as

$$A^{\text{SU}} =$$

$$\left\{ \left[\frac{1}{4}(C_{11} + C_{22} + 2C_{12})(S_{11} + S_{22} + 2S_{12}) - 1 \right]^2 \right.$$
$$+ 2\left[\frac{1}{16}(C_{11} + C_{22} - 2C_{12} + 4C_{66}) \right.$$
$$\left. \left. (S_{11} + S_{22} - 2S_{12} + S_{66})^2 \right] \right\}^{1/2}$$

$$A^{\text{Ranganathan}} = \frac{K^V}{K^R} + 2\frac{G^V}{G^R} - 3 \geq 0 \quad (2)$$

and

$$A^{\text{Kube}} = \sqrt{\left(\ln\frac{K^V}{K^R}\right)^2 + 2\left(\ln\frac{G^V}{G^R}\right)^2} \quad (3)$$

where K^V and K^R and G^V and G^R are area and shear moduli for Voigt and Reuss parameters, respectively, and expressed by the following relations[49]

$$K^V = \frac{C_{11} + C_{22} + 2C_{12}}{4}$$

$$G^V = \frac{C_{11} + C_{22} - 2C_{12} + 4C_{66}}{8}$$

$$K^R = \frac{1}{S_{11} + S_{22} + 2S_{12}}$$

$$G^R = \frac{2}{S_{11} + S_{22} - 2S_{12} + S_{66}} \quad (4)$$

where S_{ij} are the elements of the compliance matrix, which is the reciprocal of the C_{ij} matrix.[49]

For graphical visualization of the anisotropy, the Poisson's ratio $\nu(\theta)$, Young's $Y(\theta)$, and shear $G(\theta)$ moduli as functions of the direction angle ($0° \leq \theta \leq 360°$) are also calculated using[52]

$$\nu(\theta) = \frac{C_{12}\cos^4(\theta) - B\cos^2(\theta)\sin^2(\theta) + C_{12}\cos^4(\theta)}{C_{22}\cos^4(\theta) + A\cos^2(\theta)\sin^2(\theta) + C_{11}\cos^4(\theta)}$$

$$Y(\theta) = \frac{C_{11}C_{22} - C_{12}^2}{C_{22}\cos^4(\theta) + A\cos^2(\theta)\sin^2(\theta) + C_{11}\cos^4(\theta)}$$

and

$$\frac{1}{G(\theta)} = [S_{11} + S_{22} - S_{12}]\cos^2(\theta)\sin^2(\theta) +$$
$$\frac{1}{4}S_{66}[\cos^4(\theta) + \sin^4(\theta) - 2\sin^2(\theta)\cos^2(\theta)] \quad (5)$$

where $A = (C_{11}C_{22} - C_{12}^2)/C_{66} - 2C_{12}$ and $B = C_{11} + C_{22} - (C_{11}C_{22} - C_{12}^2)/C_{66}$.

We start by applying uniaxial (longitudinal ε_x and lateral ε_y) and equi-biaxial (ε_{xy}) strains. The parabolic strain energy E_s profile (Figure 2) demonstrates that the strain-free state ($\varepsilon = 0\%$) is energetically favorable within ±6% range of applied strains. The wideness of these curves suggests that the impact of the strain follows the trend $\varepsilon_x < \varepsilon_y < \varepsilon_{xy}$.

Following the above formalism, the computed values of C_{11}, C_{22}, C_{12}, and C_{66} are found to be 86.87, 136.83, −20.51, and 53.69 N/m, respectively (Table 1). The mechanical stability is
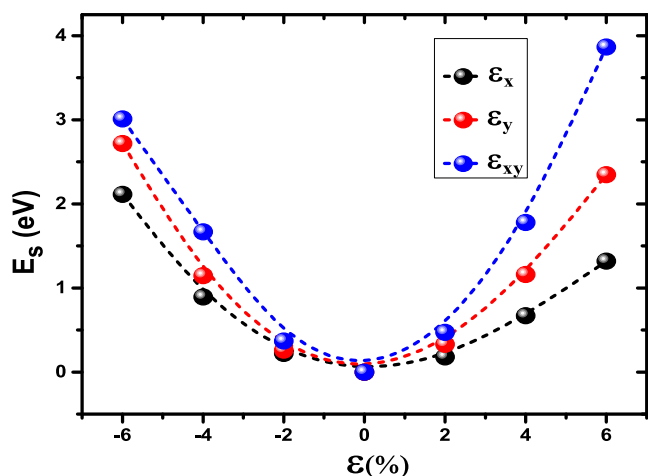
Figure 2. (Color online) the strain energy E_s (eV) as a function of different modes of strains ε.

approved by obeying the Born-Huang criteria,[53] $C_{11}C_{22} - C_{11}^2 > 0$, and $C_{66} > 0$. This ensures the positive-definiteness of $E_s(\varepsilon)$ followed by lattice distortion. The two most important mechanical parameters: 2D Young's modulus (Y) and Poisson's ratio (ν) are investigated along the (100) and (010) directions. The 2D Young's modulus for the (100) and (010) directions, $Y_a = (C_{11}C_{22} - C_{12}C_{21})/C_{22}$ and $Y_b = (C_{11}C_{22} - C_{12}C_{21})/C_{11}$, are 83.79 and 131.99 N/m, respectively, and Y_b is equivalent to that of p-SiCN.[7] The significantly lower value of Y_a not only indicates the relatively softer plane but also demonstrates a large mechanical anisotropy (LMA), which is unique from other penta monolayers.[7,9,17]

On the other hand, the Poisson's ratio in the corresponding directions ($\nu_a = C_{12}/C_{22}$ and $\nu_b = C_{12}/C_{11}$) are −0.150 and −0.236, respectively, which also supports LMA. In addition, the absolute value of the shear modulus is $G_{xy} = 53.69$ N/m, which is relatively smaller compared to that of penta-BCN.[10]

To further corroborate, the anisotropy indices are calculated to get insights into the mechanical anisotropy (Table 2). The close to zero value of the anisotropy indices denotes the isotropic elastic response, while an increased value from that reference point indicates the degree of anisotropy. The high values of A^{SU}, $A^{Ranganathan}$, and A^{Kube} indicate mechanical anisotropy, which is visualized by the polar plots (Figure 3). The orientation-dependent polar plots ($0° \leq \theta \leq 360°$) for $Y(\theta)$ and $\nu(\theta)$ show the deformed circles, justifying the presence of LMA (Figure 3a,b). However, the orientation dependency of $G(\theta)$ shows a quasi-anisotropic mechanical

response as demonstrated by the relatively small distortion from a perfect circle as shown in Figure 3c.

The maximum value of $Y_{a/b}$ and $\nu_{a/b}$ for the monolayer is located along the (010) (90°), while that of $G_{a/b}$ is located along (110) (45°). On the other hand, the minimum values of $Y_{a/b}$, $\nu_{a/b}$, and $G_{a/b}$ are at (100) (0°), (110) (45°), and (010) (90°), respectively.

Even though the negative value of C_{12} leaves the early signature of NPR, it is crucial to verify the presence of NPR. Following refs 17 and 55, a longitudinal strain along the x-axis ($\varepsilon_x = 1$, 3, and 5%) is applied, and the corresponding strain energy (E_s) is observed as a function of the lateral strain along the y-axis (ε_y). The increase in E_s and the shift of the equilibrium lattice constant with increasing ε_x confirm the presence of NPR (Figure 4). It is important to mention here that, while the theory of continuum mechanics does not preclude the possibility of inception of NPR in a stable 2D material, it is uncommon to find such rare NPR material,[17] and our first-principles prediction of NPR in p-PBN is scarce. This exceptional NPR in p-PBN is attributed to the buckled and asymmetric geometrical structure, particularly the shorter and quasi sp^3-hybridized B−N bond and the rigidity against the strain (discussed below). This exciting finding makes the monolayer a superior candidate material for multiple applications such as a tension-activatable substrate, a nano-auxetic, and a deformable variable stiffness device.

Further, high strains are loaded in a $4 \times 4 \times 1$ supercell of p-PBN along both the uniaxial ($\varepsilon_{x/y}$) and biaxial (ε_{xy}) directions to identify the ultimate bond breaking, corresponding geometrical reconstruction, and elastic−plastic region. The tensile strain is loaded with full atomic relaxation until p-PBN completely breaks and is deformed. The variations of stress, strain-energy, bond length, and thickness (buckling height) as functions of the different modes of strains applied are shown in Figures 5 and 6. With increasing ε_x, the stress increases monotonically, reaching the maximum value, the so-called ultimate stress (U_x) of 3.40 N/m at a corresponding strain $\varepsilon_c = 6\%$. The stress then starts to drop with a higher strain ($8 \leq \varepsilon_x \leq 20\%$), indicating a small elastic response of p-PBN. On the other hand, the strain energy grows exponentially until saturation at $\varepsilon_x = 16\%$. The variation of bond length and thickness (h) against ε_x describes the corresponding geometrical reconstruction. In the range $0 \leq \varepsilon_x \leq 6\%$, only the P1−B bond increases contrary to other bond lengths, including the B−P2 bond. This converse variation of longitudinal bond P1−B and lateral bond B−P2 supports the existence of NPR within 6% of strain. The small variation of the short covalent B−N bond against ε_x proves the strongest quasi sp^3-hybridized character. Furthermore, the regaining of bond length of P1−B and B−P2 and the small bond variation in the range 16% ≤ ε_x

Table 1. Elastic Constants $C_{ij=1,2,6}$ (N/m), 2D Young's Modulus $Y_{a/b}$ (N/m), and Poisson's Ratio $\nu_{a/b}$ from This Work and for Other Ternary Penta Monolayers

materials	refs	C_{11}	C_{22}	C_{12}	C_{66}	Y_a	Y_b	ν_a	ν_b
p-PBN	this work	86.87	136.83	−20.51	53.70	83.79	131.99	−0.150	−0.236
p-SiCN	ref 7	132.15	133.59	−17.44	74.80	129.88	131.29	−0.131	−0.132
p-BNSi	ref 11	114.46	112.21	12.76	48.97	113	109	0.11	0.11
p-BCN	ref 16	210.15	170.77	4.27	102.93	210.05	170.66	0.020	0.025
	ref 54	214.45	176.10	4.38	103.54	214.36	175.99	0.020	0.025
	ref 10	223.56	189.16	4.90	104.80	223.45	189.03	0.022	0.026
p-CNP	ref 9	173.32	183.57	4.52	99.01	172	190		

Table 2. Estimated Voigt and Reuss Shear (G^V and G^R) and Area (K^V and K^R) Moduli and the Elastic Anisotropic Indices (A^{SU}, $A^{Ranganathan}$, and A^{Kube}) for the p-PBN Monolayer

materials	ref	G^V	G^R	K^V	K^R	A^{SU}	$A^{Ranganathan}$	A^{Kube}
p-PBN	this work	59.93	57.87	45.67	43.31	0.0503	0.1256	0.0315
p-BCN	ref 16	98.01	97.21	97.36	96.32	0.0116	0.0273	0.0069

(a)

(b)

(c)
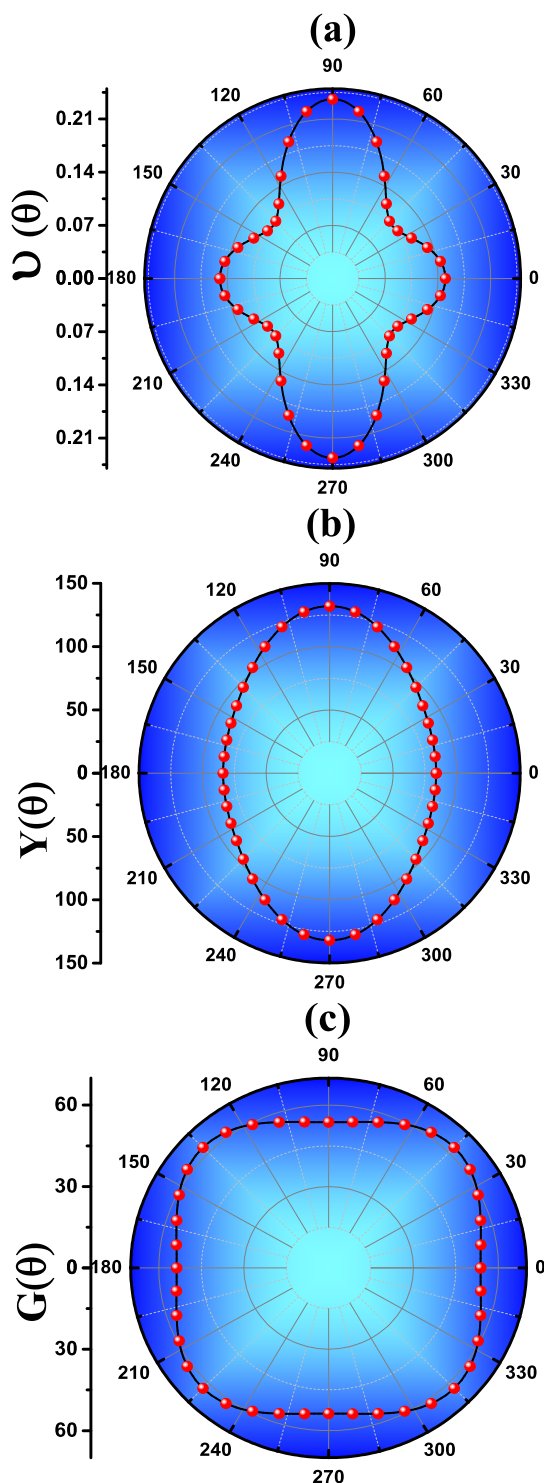
Figure 3. (Color online) the orientation dependence of (a) Poisson's ratio $\nu(\theta)$, (b) Young's modulus $Y(\theta)$, and (c) shear modulus $G(\theta)$.

Figure 4. (Color online) verification of negative Poisson's ratio—the strain energy E_s vs lateral strain ε_y with respect to longitudinal strain ε_x. Arrows show the respective energy minima.

stress and strain energy profile is observed when ε_y is applied. However, the U_y value is higher (5.79 N/m) as compared to U_x. On the other hand, all bonds seem to increase in length (except for P1−B). The continuation of contrasting bond length variation of P1−B and B−P2 within the elastic range approves the existence of NPR. A similar bond variation was detected in p-SiCN, which demonstrates the high value of NPR.[7] In addition, when the equi-biaxial strain (ε_{xy}) is applied, a similar stress and strain energy profile with an inappreciable bond lengths variation is detected until ε_{xy} reaches the ultimate value. The corresponding ultimate stress (U_{xy}) is measured to be 6.56 N/m, which is relatively higher than U_x and U_y, indicating higher strength against ε_{xy}. Beyond U_{xy}, notable bond length variations are observed. For the different strains applied, a clear drop in the monolayer thickness (h) is observed, with a drastic reduction clearly seen when the strain ε_{xy} is applied. At ε_{xy} = 20%, the thickness rockets to 1.95 Å, showing a complete deformation of p-PBN. Noting that, the ultimate stress and strain of p-PBN are relatively smaller as compared to other penta ternary[7,9−11] monolayers. The deformed structures at higher loading of strains are shown in Figure 7. It suggests that p-PBN is in the best operable phase within 6% of stretching.

Electronic Properties. To get a deep insight into the electronic behavior of p-PBN, the electronic band structure and partial density of states (PDOSs) are computed for both spin-polarized and non-polarized configurations. The symmetry in both the spin-up and spin-down channels with zero magnetic moments confirms the non-magnetic ground state of the monolayer. The high-symmetry points along the Γ−X−M−Y−Γ direction of the first Brillouin zone are chosen for band calculations (Figure 8). Interestingly, the valence band maximum (VBM) and conduction band minimum (CBM) are entwined near the Fermi level (FL) between the X−M path, demonstrating the metallic behavior of p-PBN. This metallic feature is also confirmed when the hybrid functional HSE06 is

≤ 20% demonstrate the unique geometrical reconstruction and justify the stress drop and strain energy saturation. A similar
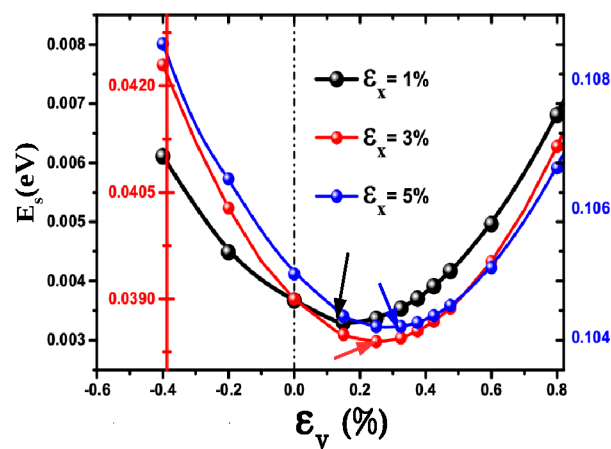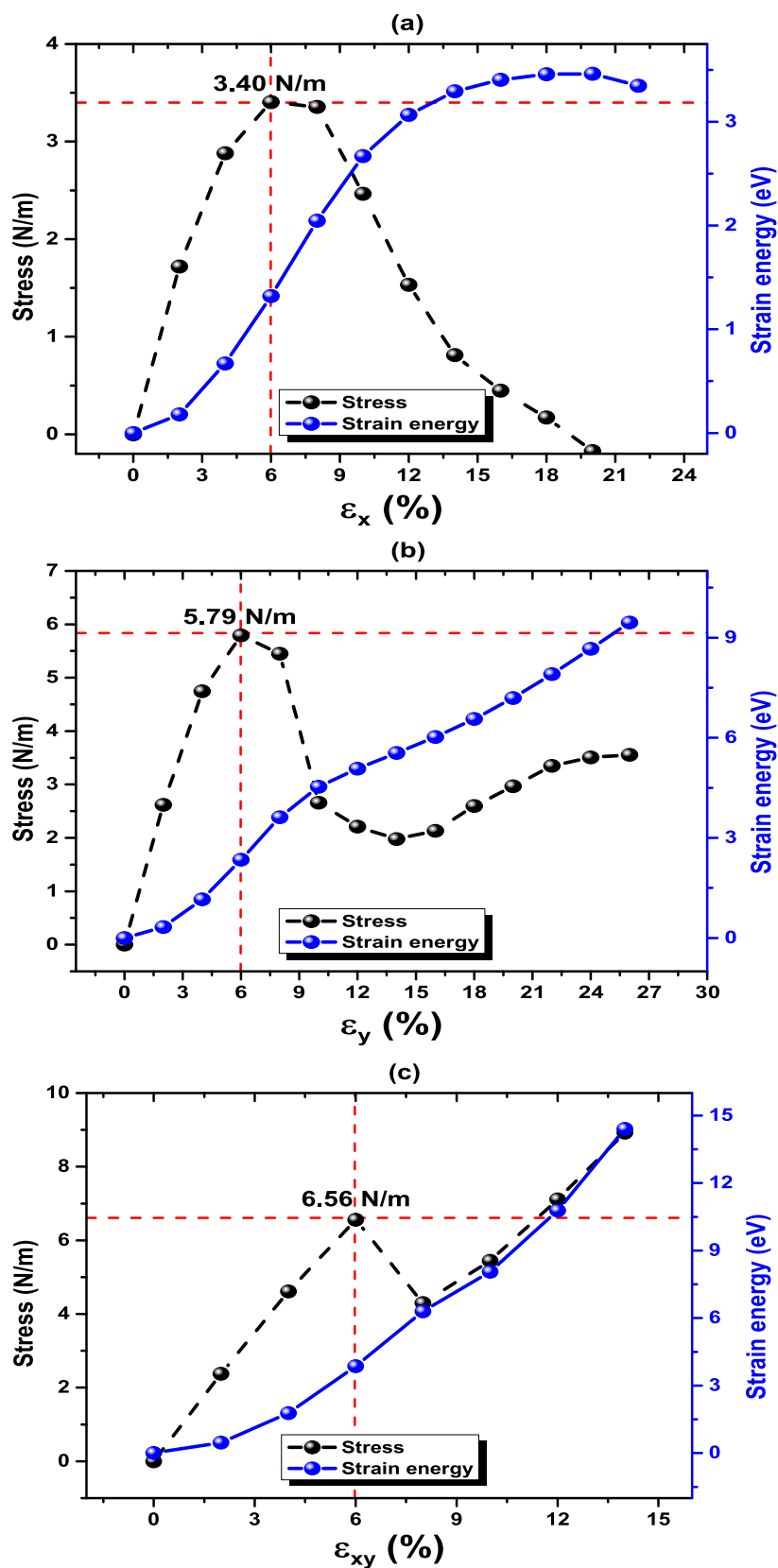
Figure 5. (Color online) the stress and strain energy as functions of uniaxial strain along the (a) *x*-direction, (b) *y*-direction, and (c) biaxial strain (along the *xy*-direction). The red dashed horizontal and vertical lines denote the ultimate stress (*U*) and corresponding strain ε_c values, respectively.

employed. See Figure S1 in the online Supporting Information. In addition, the PDOS plot, as obtained by both Perdew−

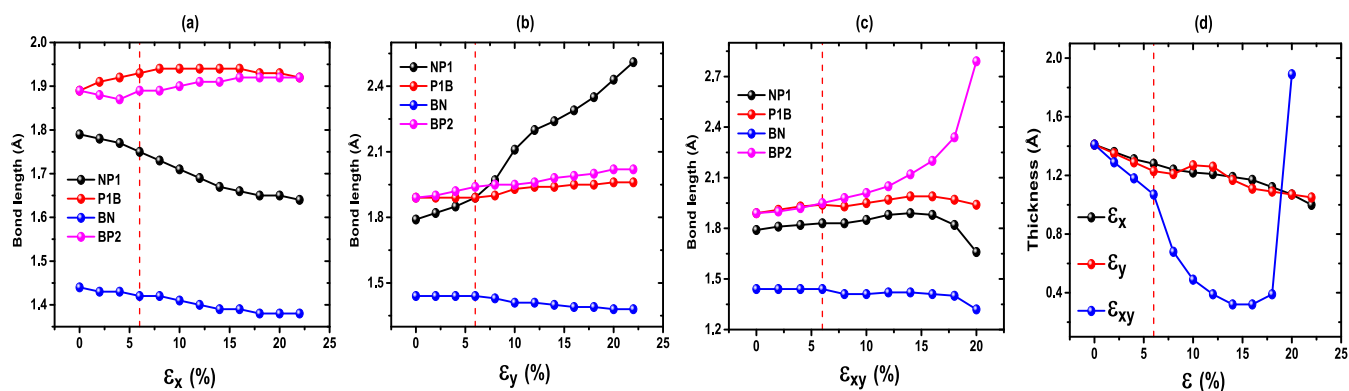Burke−Ernzerhof (PBE) and HSE06 functionals, confirms that the B-2p, N-2p, and P-3p with B-2s electronic orbitals (sp^3-

Figure 6. (Color online) the variation of bond lengths with (a) uniaxial strain along the *x*-direction, (b) uniaxial strain along the *y*-direction, (c) biaxial strain along the *xy*-direction, and (d) variation of monolayer thickness (*h*) with different modes of strains.
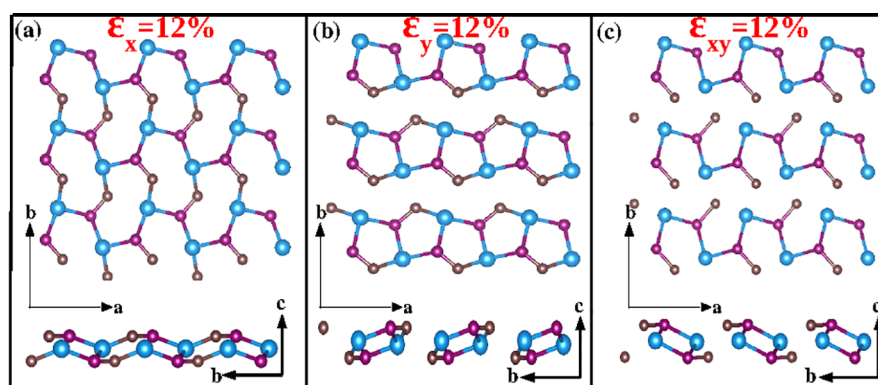

Figure 7. (Color online) the deformed structures at 12% of (a) uniaxial strain along the *x*-direction, (b) uniaxial strain along the *y*-direction, and (c) biaxial strain along the *xy*-direction beyond $\varepsilon_c = 6\%$ for *p*-PBN.
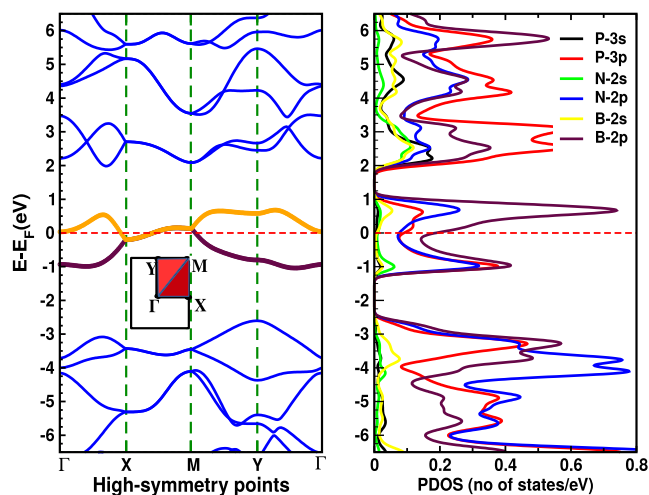

Figure 8. (Color online) the electronic band structure with a schematic sketch of high-symmetry points in the first Brillouin zone (left) and partial density of states (right) for *p*-PBN.

hybridized) contribute in descending order in the vicinity of the FL. Furthermore, both the uniaxial and biaxial strains are loaded to examine the metallicity. Nevertheless, only minor shifting of the VBM and CBM from the FL is observed, suggesting the rigid metallicity of *p*-PBN. This remarkable electronic response was also detected in the auxetic *p*-SiCN monolayer, but it is different from other penta iso-structures. This rigid metallicity is highly desirable for the fabrications of

electrode materials in high-performance lithium-ion batteries and high-quality electronic devices.

CONCLUSIONS

In summary, using first-principles density functional theory (DFT) calculations, a new pentagonal monolayer *p*-PBN is predicted, which is structurally, chemically, mechanically, dynamically, thermodynamically stable, and experimentally feasible. The new *p*-PBN exhibits metallic behavior, which is preserved even under high strains. Remarkably, the short and strong quasi sp³-hybridized B−N bond and unique bond variation and geometrical reconstruction with applied strain allow *p*-PBN to possess a high NPR value, the highest among all the ternary penta iso-structures. The large difference between the (100) and (010) directions' Young's modulus and Poisson's ratio values demonstrate the large anisotropic mechanics of the monolayer. Nevertheless, because of the unique geometrical reconstruction against the strain, the monolayer is sustainable and operable up to 6% of stretching. Our findings not only introduce a new ternary monolayer but also pave the way for future possibilities of experimental fabrication and characterization of modern nanoscale electro-mechanical devices based on auxetic nanomaterials and nanostructures.

COMPUTATIONAL METHODS

In this work, the DFT implemented in the Spanish Initiative for Electronic Simulations with Thousands of Atoms (SIESTA)[56,57] is used for electronic structure calculations.

The semi-local forms of norm-conserving pseudopotentials[58] are utilized to determine the interaction between ions and electrons. The generalized gradient approximation of PBE,[59] within the double zeta plus polarization basis sets, is used to determine the exchange-correlation potential. A $20 \times 20 \times 1$ k-points within the Monkhorst pack scheme,[60] and 350 Rydberg cutoff energy are set to meet the convergence criteria. The atomic force of 0.002 eV/Å and self-consistent field of 10^{-6} eV are set for tight convergence within the conjugate-gradient scheme. In addition, a vacuum-gap separation of 25 Å is used along the z-axis of the monolayer to avoid unnecessary interlayer interactions. The chemical stability and strength are checked by analyzing the cohesive E_c and formation E_f energies. The frozen phonon method, implemented in the Vibra utility of SIESTA, is used for the phonon dispersion calculation and dynamical stability test. A large supercell of $6 \times 6 \times 1$ is converged to obtain an accurate force matrix. Furthermore, to account for the thermal stability, the Viena Ab-initio Simulation Package[61] is utilized to perform the AIMD simulations with a $6 \times 6 \times 1$ supercell used for convergence.

ASSOCIATED CONTENT

Supporting Information

The Supporting Information is available free of charge at https://pubs.acs.org/doi/10.1021/acsomega.2c03567.

> Lattice parameters and coordinates of the optimized geometry for p-PBN in the POSCAR format and the PDOSs confirming the metallic behavior of p-PBN as obtained using the HSE06 functional (PDF)

AUTHOR INFORMATION

Corresponding Authors

Shambhu Bhandari Sharma − *Department of Physics, Khalifa University of Science and Technology, Abu Dhabi 127788, United Arab Emirates;* ⓘ orcid.org/0000-0002-6003-7425; Email: shambhu.sharma@ku.ac.ae

Issam A. Qattan − *Department of Physics, Khalifa University of Science and Technology, Abu Dhabi 127788, United Arab Emirates;* Email: issam.qattan@ku.ac.ae

Authors

Santosh KC − *Chemical and Materials Engineering, San Jose State University, San Jose, California 95112, United States*

Ahmad M. Alsaad − *Department of Physical Sciences, Jordan University of Science and Technology, Irbid 22110, Jordan;* ⓘ orcid.org/0000-0003-1721-1878

Complete contact information is available at:
https://pubs.acs.org/10.1021/acsomega.2c03567

Notes

The authors declare no competing financial interest.

ACKNOWLEDGMENTS

REFERENCES

(1) Shen, Y.; Wang, Q. Pentagon-based 2D materials: Classification, properties and applications. *Phys. Rep.* **2022**, *964*, 1−42.

(2) Nazir, M. A.; Hassan, A.; Shen, Y.; Wang, Q. Research progress on penta-graphene and its related materials: Properties and applications. *Nano Today* **2022**, *44*, 101501.

(3) Prévot, G.; Hogan, C.; Leoni, T.; Bernard, R.; Moyen, E.; Masson, L. Si nanoribbons on Ag (110) studied by grazing-incidence x-ray diffraction, scanning tunneling microscopy, and density-functional theory: evidence of a pentamer chain structure. *Phys. Rev. Lett.* **2016**, *117*, 276102.

(4) Sheng, S.; Ma, R.; Wu, J.-b.; Li, W.; Kong, L.; Cong, X.; Cao, D.; Hu, W.; Gou, J.; Luo, J.-W.; Cheng, P.; Tan, P.-H.; Jiang, Y.; Chen, L.; Wu, K. The pentagonal nature of self-assembled silicon chains and magic clusters on Ag (110). *Nano Lett.* **2018**, *18*, 2937−2942.

(5) Cerdá, J. I.; Sławińska, J.; Le Lay, G.; Marele, A. C.; Gómez-Rodríguez, J. M.; Dávila, M. E. Unveiling the pentagonal nature of perfectly aligned single-and double-strand Si nano-ribbons on Ag (110). *Nat. Commun.* **2016**, *7*, 13076.

(6) Chow, W. L.; Yu, P.; Liu, F.; Hong, J.; Wang, X.; Zeng, Q.; Hsu, C.-H.; Zhu, C.; Zhou, J.; Wang, X.; Xia, J.; Yan, J.; Chen, Y.; Wu, D.; Yu, T.; Shen, Z.; Lin, H.; Jin, C.; Tay, B. K.; Liu, Z. High mobility 2D palladium diselenide field-effect transistors with tunable ambipolar characteristics. *Adv. Mater.* **2017**, *29*, 1602969.

(7) Sharma, S. B.; Qattan, I. A.; Jaishi, M.; Paudyal, D. Penta-SiCN: A Highly Auxetic Monolayer. *ACS Appl. Electron. Mater.* **2022**, *4*, 2561−2569.

(8) Zhang, S.; Zhou, J.; Wang, Q.; Jena, P. Beyond graphitic carbon nitride: nitrogen-rich penta-CN2 sheet. *J. Phys. Chem. C* **2016**, *120*, 3993−3998.

(9) Sun, W.; Shen, Y.; Guo, Y.; Chen, Y.; Wang, Q. 1, 2, 4-Azadiphosphole-based piezoelectric penta-CNP sheet with high spontaneous polarization. *Appl. Surf. Sci.* **2021**, *554*, 149499.

(10) Zhao, K.; Guo, Y.; Shen, Y.; Wang, Q.; Kawazoe, Y.; Jena, P. Penta-BCN: A New Ternary Pentagonal Monolayer with Intrinsic Piezoelectricity. *J. Phys. Chem. Lett.* **2020**, *11*, 3501−3506.

(11) Varjovi, M. J.; Kilic, M.; Durgun, E. Ternary pentagonal BNSi monolayer: Two-dimensional structure with potentially high carrier mobility and strong excitonic effects for photocatalytic applications. *Phys. Rev. Mater.* **2022**, *6*, 034004.

(12) Azarmi, Z.; Naseri, M.; Parsamehr, S. Penta-BeP2 monolayer: A new 2D beryllium phosphate with a narrow band gap. *Chem. Phys. Lett.* **2019**, *728*, 136−141.

(13) Kumar, V.; Dey, A.; Thomas, S.; Asle Zaeem, M. A.; Roy, D. R. Hydrogen-induced tunable electronic and optical properties of a two-dimensional penta-Pt 2 N 4 monolayer. *Phys. Chem. Chem. Phys.* **2021**, *23*, 10409−10417.

(14) Novoselov, K. S.; Fal'ko, L.; Colombo, P.; Gellert, M.; Schwab, K.; Kim, K. A roadmap for graphene. *Nature* **2012**, *490*, 192−200.

(15) Oyedele, A. D.; Yang, S.; Liang, L.; Puretzky, A. A.; Wang, K.; Zhang, J.; Yu, P.; Pudasaini, P. R.; Ghosh, A. W.; Liu, Z.; Rouleau, C. M.; Sumpter, B. G.; Chisholm, M. F.; Zhou, W.; Rack, P. D.; Geohegan, D. B.; Xiao, K. PdSe2: pentagonal two-dimensional layers with high air stability for electronics. *J. Am. Chem. Soc.* **2017**, *139*, 14090−14097.

(16) Sharma, S. B.; Bhatta, R.; Adhikari, R.; Paudyal, D. Strain dependent electronic and optical responses of penta-BCN monolayer. *Carbon Trends* **2022**, *7*, 100162.

(17) Zhang, S.; Zhou, J.; Wang, Q.; Chen, X.; Kawazoe, Y.; Jena, P. Penta-graphene: A new carbon allotrope. *Proc. Natl. Acad. Sci.* **2015**, *112*, 2372−2377.

(18) Peng, R.; Ma, Y.; Wu, Q.; Huang, B.; Dai, Y. Two-dimensional materials with intrinsic auxeticity: progress and perspectives. *Nanoscale* **2019**, *11*, 11413−11428.

(19) Liu, G.; Zeng, Q.; Zhu, P.; Quhe, R.; Lu, P. Negative Poisson's ratio in monolayer PdSe2. *Comput. Mater. Sci.* **2019**, *160*, 309−314.

(20) Yagmurcukardes, M.; Sahin, H.; Kang, J.; Torun, E.; Peeters, F. M.; Senger, R. T. Pentagonal monolayer crystals of carbon, boron nitride, and silver azide. *J. Appl. Phys.* **2015**, *118*, 104303.

(21) Li, X.; Qiang, X.; Gong, Z.; Zhang, Y.; Gong, P.; Chen, L. Tunable Negative Poisson's Ratio in Van der Waals Superlattice. *Research* **2021**, *2021*, 1904839.

(22) Ma, X.; Liu, J.; Fan, Y.; Li, W.; Hu, J.; Zhao, M. Giant negative Poisson's ratio in two-dimensional V-shaped materials. *Nanoscale Adv.* **2021**, *3*, 4554–4560.

(23) Alderson, A.; Alderson, K. Auxetic materials. *Proc. Inst. Mech. Eng., Part G* **2007**, *221*, 565–575.

(24) Yang, W.; Li, Z.-M.; Shi, W.; Xie, B.-H.; Yang, M.-B. Review on auxetic materials. *J. Mater. Sci.* **2004**, *39*, 3269–3279.

(25) Huang, C.; Chen, L. Negative Poisson's ratio in modern functional materials. *Adv. Mater.* **2016**, *28*, 8079–8096.

(26) Choi, J. B.; Lakes, R. S. Design of a fastener based on negative Poisson's ratio foam. *Cell. Polym.* **1991**, *10*, 205–212.

(27) Avellaneda, M.; Swart, P. J. Calculating the performance of 1–3 piezoelectric composites for hydrophone applications: an effective medium approach. *J. Acoust. Soc. Am.* **1998**, *103*, 1449–1467.

(28) Lakes, R. Foam structures with a negative Poisson's ratio. *Science* **1987**, *235*, 1038–1040.

(29) Greaves, G. N.; Greer, A. L.; Lakes, R. S.; Rouxel, T. Poisson's ratio and modern materials. *Nat. Mater.* **2011**, *10*, 823–837.

(30) Scarpa, F. Auxetic materials for bioprostheses [In the Spotlight]. *IEEE Signal Process. Mag.* **2008**, *25*, 128.

(31) Kong, X.; Deng, J.; Li, L.; Liu, Y.; Ding, X.; Sun, J.; Liu, J. Z. Tunable auxetic properties in group-IV monochalcogenide monolayers. *Phys. Rev. B* **2018**, *98*, 184104.

(32) Gibson, I.; Ashby, M. F. The mechanics of three-dimensional cellular materials. *Proc. R. Soc. London, Ser. A* **1982**, *382*, 43–59.

(33) Du, Y.; Maassen, J.; Wu, W.; Luo, Z.; Xu, X.; Ye, P. D. Auxetic black phosphorus: a 2D material with negative Poisson's ratio. *Nano Lett.* **2016**, *16*, 6701–6708.

(34) Jiang, J.-W.; Park, H. S. Negative poisson's ratio in single-layer black phosphorus. *Nat. Commun.* **2014**, *5*, 4727.

(35) Kou, L.; Ma, Y.; Tang, C.; Sun, Z.; Du, A.; Chen, C. Auxetic and ferroelastic borophane: a novel 2D material with negative Possion's ratio and switchable dirac transport channels. *Nano Lett.* **2016**, *16*, 7910–7914.

(36) Han, J.; Xie, J.; Zhang, Z.; Yang, D.; Si, M.; Xue, D. Negative Poisson's ratios in few-layer orthorhombic arsenic: First-principles calculations. *Appl. Phys. Express* **2015**, *8*, 041801.

(37) Zhou, L.; Zhuo, Z.; Kou, L.; Du, A.; Tretiak, S. Computational dissection of two-dimensional rectangular titanium mononitride TiN: auxetics and promises for photocatalysis. *Nano Lett.* **2017**, *17*, 4466–4472.

(38) Wang, Y.; Li, F.; Li, Y.; Chen, Z. Semi-metallic Be 5 C 2 monolayer global minimum with quasi-planar pentacoordinate carbons and negative Poisson's ratio. *Nat. Commun.* **2016**, *7*, 11488.

(39) Wang, Y.; Li, F.; Li, Y.; Chen, Z. Semi-metallic Be 5 C 2 monolayer global minimum with quasi-planar pentacoordinate carbons and negative Poisson's ratio. *Nat. Commun.* **2016**, *7*, 11488.

(40) Guo, Y.; Zhou, J.; Xie, H.; Chen, Y.; Wang, Q. Screening transition metal-based polar pentagonal monolayers with large piezoelectricity and shift current. *npj Comput. Mater.* **2022**, *8*, 40.

(41) Chen, Q.-Y.; Liu, M.-y.; Cao, C.; He, Y. Anisotropic optical properties induced by uniaxial strain of monolayer C 3 N: a first-principles study. *RSC Adv.* **2019**, *9*, 13133–13144.

(42) Liu, S.; Liu, B.; Shi, X.; Lv, J.; Niu, S.; Yao, M.; Li, Q.; Liu, R.; Cui, T.; Liu, B. Two-dimensional penta-BP 5 sheets: High-stability, strain-tunable electronic structure and excellent mechanical properties. *Sci. Rep.* **2017**, *7*, 2404.

(43) Sharma, S. B.; Bhatta, R.; Sigdel, K. R.; Adhikari, R. P.; Kaphle, G. C. Structural, electronic, magnetic and mechanical properties of vanadium-doped boron nitride monolayer. *Eur. Phys. J. B* **2021**, *94*, 128.

(44) Amorim, R. G.; Zhong, X.; Mukhopadhyay, S.; Pandey, R.; Rocha, A. R.; Karna, S. P. Strain-and electric field-induced band gap modulation in nitride nanomembranes. *J. Condens. Matter Phys.* **2013**, *25*, 195801.

(45) Topsakal, M.; Aktürk, E.; Ciraci, S. First-principles study of two-and one-dimensional honeycomb structures of boron nitride. *Phys. Rev. B: Condens. Matter Mater. Phys.* **2009**, *79*, 115442.

(46) Marianetti, C. A.; Yevick, H. G. Failure mechanisms of graphene under tension. *Phys. Rev. Lett.* **2010**, *105*, 245502.

(47) Si, C.; Duan, W.; Liu, Z.; Liu, F. Electronic strengthening of graphene by charge doping. *Phys. Rev. Lett.* **2012**, *109*, 226802.

(48) Andrew, R.; Mapasha, R.; Ukpong, A.; Chetty, N. Erratum: Mechanical properties of graphene and boronitrene [Phys. Rev. B 85, 125428 (2012)]. *Phys. Rev. B* **2019**, *100*, 209901.

(49) Li, R.; Shao, Q.; Gao, E.; Liu, Z. Elastic anisotropy measure for two-dimensional crystals. *Extreme Mech. Lett.* **2020**, *34*, 100615.

(50) Ranganathan, S. I.; Ostoja-Starzewski, M. Universal elastic anisotropy index. *Phys. Rev. Lett.* **2008**, *101*, 055504.

(51) Kube, C. M.; de Jong, M. Elastic constants of polycrystals with generally anisotropic crystals. *J. Appl. Phys.* **2016**, *120*, 165105.

(52) Chen, S.-B.; Zeng, Z.-Y.; Chen, X.-R.; Yao, X.-X. Strain-induced electronic structures, mechanical anisotropy, and piezoelectricity of transition-metal dichalcogenide monolayer CrS2. *J. Appl. Phys.* **2020**, *128*, 125111.

(53) Born, M.; Misra, R. D.On the stability of crystal lattices. IV. *Mathematical Proceedings of the Cambridge Philosophical Society*, 1940; pp 466–478.

(54) Dabsamut, K.; Thanasarnsurapong, T.; Maluangnont, T.; T-Thienprasert, T.; Jungthawan, S.; Boonchun, A. Strain engineering and thermal conductivity of a penta-BCN monolayer: a computational study. *J. Phys. D: Appl. Phys.* **2021**, *54*, 355301.

(55) Wang, B.; Wu, Q.; Zhang, Y.; Ma, L.; Wang, J. Auxetic B4N monolayer: a promising 2D material with in-plane negative Poisson's ratio and large anisotropic mechanics. *ACS Appl. Mater. Interfaces* **2019**, *11*, 33231–33237.

(56) Soler, J. M.; Artacho, E.; Gale, J. D.; García, A.; Junquera, J.; Ordejón, P.; Sánchez-Portal, D. The SIESTA method for ab initio order-N materials simulation. *J. Condens. Matter Phys.* **2002**, *14*, 2745.

(57) Artacho, E.; Sánchez-Portal, D.; Ordejón, P.; Garcia, A.; Soler, J. M. Linear-scaling ab-initio calculations for large and complex systems. *Phys. Status Solidi B* **1999**, *215*, 809–817.

(58) Troullier, N.; Martins, J. L. Efficient pseudopotentials for plane-wave calculations. *Phys. Rev. B: Condens. Matter Mater. Phys.* **1991**, *43*, 1993.

(59) Perdew, J. P.; Burke, K.; Ernzerhof, M. Generalized gradient approximation made simple. *Phys. Rev. Lett.* **1996**, *77*, 3865.

(60) Monkhorst, H. J.; Pack, J. D. Special points for Brillouin-zone integrations. *Phys. Rev. B: Solid State* **1976**, *13*, 5188.

(61) Kresse, G.; Joubert, D. From ultrasoft pseudopotentials to the projector augmented-wave method. *Phys. Rev. B: Condens. Matter Mater. Phys.* **1999**, *59*, 1758.